

CT3D++: Improving 3D Object Detection with Keypoint-induced Channel-wise Transformer

Hualian Sheng · Sijia Cai · Na Zhao · Bing Deng · Qiao Liang ·
Min-Jian Zhao · Jieping Ye

Received: date / Accepted: date

Abstract The field of 3D object detection from point clouds is rapidly advancing in computer vision, aiming to accurately and efficiently detect and localize objects in three-dimensional space. Current 3D detectors commonly fall short in terms of flexibility and scalability, with ample room for advancements in performance. In this paper, our objective is to address these limitations by introducing two frameworks for 3D object detection with minimal hand-crafted design. Firstly, we propose CT3D, which sequentially performs raw-point-based embedding, a standard Transformer encoder, and a channel-wise decoder for point features within each proposal. Secondly, we present an enhanced network called CT3D++, which incorporates geometric and semantic fusion-based embedding to extract more valuable and comprehensive proposal-aware information. Additionally, CT3D++ utilizes a point-to-key bidirectional encoder for more efficient feature encoding with reduced computational cost. By replacing the corresponding components of CT3D with these novel modules, CT3D++ achieves state-of-the-art performance on both the KITTI dataset and the large-scale Waymo Open Dataset. The

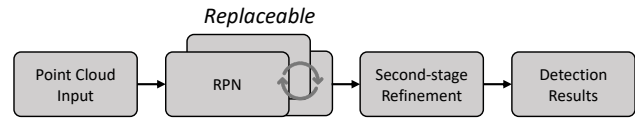


Fig. 1 General point cloud-based 3D object detection framework. We advocate to design flexible architecture with replaceable RPN.

source code for our frameworks will be made accessible at <https://github.com/hlsheng1/CT3D-plusplus>.

Keywords 3D object detection · Point clouds · Transformer · Geometric and semantic fusion

1 Introduction

3D object detection is a fundamental technology required for autonomous driving, which plays a vital role in driving decision-making and safety assurance. Many methods Deng et al. (2021); Sheng et al. (2021); Shi et al. (2020a); Yin et al. (2021); Li et al. (2021); Xu et al. (2022); He et al. (2022) adopt a two-stage strategy that adds one extra refinement network based on the single-stage methods Lang et al. (2019); Sheng et al. (2022); Yan et al. (2018); Zheng et al. (2021); He et al. (2020) to achieve better performance. The main objective for the second-stage network is to effectively model the differences between the 3D proposals and ground-truths, and the main bottleneck is how to effectively extract the proposal-aware features.

Currently, refinement in two-stage methods Shi et al. (2020a, 2023); Deng et al. (2021); Li et al. (2021) primarily relies on the PointNet Qi et al. (2017a) technique, which employs a flexible receptive field to aggregate features from the first-stage layers through a permutation-

Hualian Sheng · Sijia Cai · Bing Deng · Qiao Liang · Jieping Ye

Alibaba Cloud, Hangzhou 310052, China
E-mail: {hualian.shl; stephen.csj; dengbing.db; chongchuan.lq; yejieping.ye}@alibaba-inc.com

Na Zhao
Information Systems Technology and Design Pillar, Singapore
University of Technology and Design, 487372, Singapore
E-mail: na.zhao@sutd.edu.sg

Min-Jian Zhao
College of Information Science and Electronic Engineering,
Zhejiang University, Hangzhou 310027, China
E-mail: mjzhao@zju.edu.cn

invariant network. However, these methods suffer from certain drawbacks due to their reliance on numerous hand-crafted designs, such as the neighbor-ball radii and grid size. Furthermore, these methods are tightly coupled with specific Region Proposal Network (RPN) architectures (such as SECOND Yan et al. (2018)), which include sparse convolution layers and conveniently provide mid-layer 3D voxel features Shi et al. (2020a, 2023); Deng et al. (2021). Without utilizing 3D voxel features, the performance of the refinement network is notably poor Deng et al. (2021); Li et al. (2021). However, practical industry applications often require architectures that do not rely on 3D voxel features. Consequently, there is a need for a network structure that combines high performance with flexibility.

This paper aims to explore a more effective two-stage framework for 3D object detection that achieves high-quality refinement of 3D proposals while eliminating dependencies on specific RPN architectures. Taking inspiration from the Transformer network Vaswani et al. (2017), which excels at modeling unordered data formats, we propose a novel framework that enhances 3D object detection performance and enables the replacement of RPN with improved versions of the standard Transformer, as shown in Figure 1. Hence, we introduce a unified framework called CT3D/CT3D++, which leverages a novel channel-wise Transformer and a novel keypoint-induced channel-wise Transformer, respectively. Through our experiments, we demonstrate the effectiveness of our proposed methods in processing point cloud features, challenging previous conclusions regarding the necessity of using 3D voxel features for refinement based on PointNet Qi et al. (2017a).

Firstly, we propose CT3D, an initial two-stage 3D object detection framework that only uses the raw point cloud in the second-stage network. This framework incorporates an arbitrary RPN to generate 3D proposals, followed by extracting per-proposal features from the raw point cloud. The second-stage network, referred to as the channel-wise Transformer, consists of three steps. Firstly, we propose a raw-point-based embedding to integrate proposal information into the raw points. Secondly, a standard Transformer encoder with a self-attention scheme is employed to capture point-wise interactions. Lastly, we introduce a novel channel-wise re-weighting approach to enhance the standard Transformer decoder for aggregating the encoded point features. This novel approach takes into consideration both global and local channel-wise features, resulting in improved expressiveness when assigning attention weights during query-key interactions. These three steps ensure the scalability of the 3D object detection framework while significantly enhancing detection performance.

Secondly, we propose an advanced 3D object detection framework called CT3D++. This framework is built upon CT3D and aims to generate more accurate detection results while reducing computational costs. Previous studies, such as PV-RCNN Shi et al. (2020a) and Voxel-RCNN Deng et al. (2021), have highlighted that an excessive reliance on multi-scale 3D voxel features in the initial stage for gathering semantic information can impede model scalability and flexibility. Instead, an alternative and improved approach is to leverage other latent space features, such as Bird’s Eye View (BEV) features. However, these investigations Shi et al. (2020a); Deng et al. (2021); Yin et al. (2021) have shown limited performance improvement when using BEV features. Therefore, we examine the combination of raw point geometric features and BEV semantic features to construct our refinement network, ensuring scalability, flexibility, and efficiency. Furthermore, in Section 5.5, we present ablation studies to demonstrate the redundancy of multi-scale 3D voxel features in our framework.

In the second stage of CT3D+++, we introduce the keypoint-induced channel-wise Transformer. This updated version incorporates enhancements to the embedding and encoder modules compared to its predecessor in CT3D. To expedite the process of raw point sampling, we propose a category-aware strategy that ensures a fixed capture area for points belonging to the same category. These sampled raw points are then projected onto the BEV feature map of the RPN, facilitating the extraction of abundant semantic information. In addition, we introduce a lightweight MLP network, comprising only a few hundred units, that operates on the concatenated geometric and semantic features. This integration significantly enhances the performance of object detection. Numerous existing studies have explored various networks, including PointNet Li et al. (2021), Self-attention Sheng et al. (2021), and Convolutional Neural Network (CNN) Shi et al. (2020a); Deng et al. (2021), to process fused features and generate the final output. However, these approaches lack efficient modeling of the relationship between the extracted features and the coarse 3D proposals, leading to diminished performance or high resource costs. Notably, the self-attention scheme exhibits quadratic computational complexity Wang et al. (2020). To address this concern, we propose a more efficient and computationally economical alternative named as the point-to-key bidirectional cross-attention (PBC) scheme. In this scheme, we compute the correlation matrix between the raw points and the key points of the coarse 3D proposals, employing it as bidirectional attention weights to simultaneously update the raw and key point features. Our PBC scheme effectively models the interactions between raw points

and key points while significantly reducing computational complexity compared to the self-attention scheme. Moreover, we validate in Section 5.5 that our proposed scheme demonstrates superior performance.

This work makes several **key contributions**: (1). We introduce the CT3D framework, which includes two innovative modules: a raw-point-based embedding module for aggregating proposal information around each point, and a channel-wise re-weighting approach for more effective refinement of feature expression. (2). We propose the CT3D++ framework, which incorporates two novel modules: a channel-wise attention-based fusion strategy for efficient combination of geometric and semantic features, and a point-to-key bidirectional cross-attention scheme that significantly reduces computational costs compared to the self-attention scheme while improving 3D bounding box refinement performance. (3). Our CT3D/CT3D++ frameworks can be seamlessly integrated into existing RPNs, resulting in significant performance enhancements. (4). Experimental results demonstrate that our CT3D/CT3D++ frameworks achieve state-of-the-art performance on both the Waymo Open Dataset and KITTI benchmark.

2 Related Work

2.1 3D Object Detection from Image.

Existing methods for 3D object detection from images can be broadly classified into two branches. The first branch focuses on monocular 3D object detection, where a single image is used to generate real-world bounding box information. The second branch is dedicated to multi-view 3D object detection, which relies on predictions from multiple images to estimate bounding boxes.

2.1.1 Monocular 3D object detection

One approach in the field of monocular 3D object detection involves generating dense depth maps for image pixels, which are then used to estimate object-wise depth values. Several studies, such as AM3D Ma et al. (2019), PatchNet Ma et al. (2020), Pseudo-LiDAR Wang et al. (2019), and PCT Wang et al. (2021a), have attempted to convert image pixels into pseudo point clouds using depth maps obtained from existing depth estimators Cao et al. (2017); Song et al. (2021); Chen et al. (2021), combined with camera information. These pseudo point clouds are subsequently utilized by point cloud-based detectors to achieve 3D object detection. Specifically, the Pseudo-LiDAR approach Wang et al. (2019) employs generated depth maps as a substitute for actual

point clouds. Alternatively, several other studies, including D⁴LCN Ding et al. (2020), Liu et al. (2021b), CaDDN Reading et al. (2021), and MonoDETR Zhang et al. (2023), opt to combine depth maps with image features to produce the final 3D detection results. This approach relies on pixel-wise depth prediction, which has the potential to enhance 3D object detection. However, it may also pose challenges in terms of generalization. Another group of studies bypasses the generation of pixel-wise depth information. Earlier works, such as SMOKE Liu et al. (2020) and FCOS3D Wang et al. (2021b), transform 2D object detectors into 3D object detectors by incorporating an additional depth estimation branch. However, their performance improvement is limited by the difficulties associated with long-range depth value predictions. Subsequently, numerous studies have focused on developing more efficient approaches to constrain the depth of object centers. Examples include MonoRCNN Shi et al. (2021), Monoflex Zhang et al. (2021), GUPNet Lu et al. (2021), MonoPair Chen et al. (2020), MonoCon Liu et al. (2021a), and PDR Sheng et al. (2023). These approaches leverage geometric information, such as prior knowledge or object relationships, resulting in significantly improved 3D object detection performance. Importantly, this group of methods typically requires fewer computational resources, making it the prevailing approach in current monocular 3D object detection technology.

2.1.2 Multi-view 3D object detection

Multi-view 3D object detection has recently garnered significant attention for its ability to perform scene understanding using multiple surrounding cameras. Typically, this approach involves transforming image features from different camera views into explicit or implicit BEV feature maps. In explicit BEV-based methods, dense BEV feature maps are constructed using specific feature assignment strategies. Approaches like Lift-splat Phillion and Fidler (2020), BEVDet Huang et al. (2021), and BEVDepth Li et al. (2023) spread image features onto the BEV map using predicted pixel-wise depth distributions. BEVFormer Li et al. (2022) and BEVFormerV2 Yang et al. (2023) aggregate image features through cross attention Vaswani et al. (2017) between dense BEV features and image features. EVFormer Li et al. (2022), BEVFormerV2 Yang et al. (2023), and BEVDet4D Huang and Huang (2022) further incorporate temporal fusion by leveraging previous BEV frame information within the BEV feature map. Implicit BEV-based methods, on the other hand, typically follow the strategy of predicting sparse location queries in BEV space, inspired by DETR Carion et al. (2020) technology.

These methods then perform cross attention between these sparse BEV queries and image features to generate query-wise feature representations. Examples of such methods include DETR3D Wang et al. (2022), Sparse-BEV Liu et al. (2023a), and the PETR series Liu et al. (2022, 2023b). The implementation of cross attention in these studies may vary, primarily due to differences in feature sensing ranges and the utilization of distinct position embeddings.

2.2 3D Object Detection from Point Cloud.

In this section, we provide a brief review of closely related works in 3D detection based on LiDAR, categorized into single-stage and two-stage pipelines. Furthermore, we discuss works that leverage the Transformer architecture.

2.2.1 Single-stage 3D object detection from point cloud

Single-stage 3D detectors employ single-shot pipelines for efficient object detection. Typically, these methods perform 3D object detection on compressed Bird’s Eye View (BEV) feature maps Yan et al. (2018); Lang et al. (2019); He et al. (2020); Sheng et al. (2022); Yang et al. (2020). Early approaches transform the 3D sparse point cloud data into compact 2D or 3D formats, such as range view-based methods Chai et al. (2021); Fan et al. (2021); Liang et al. (2021), BEV view-based methods Chen et al. (2017); Ku et al. (2018), and dense volume-based methods Li (2017); Yang et al. (2018); Zhou and Tuzel (2018). Subsequently, traditional 2D/3D CNNs are employed to extract features. However, these methods often suffer from information loss or high computational costs. To address these challenges, SECOND Yan et al. (2018) introduces 3D sparse convolution to reduce the computational complexity associated with dense volume-based methods, while maintaining high efficiency. Building upon this, PointPillar Lang et al. (2019) replaces 3D sparse convolution with PointNet-like Qi et al. (2017a) feature extraction for each "pillar," resulting in faster detection speeds. SA-SSD He et al. (2020) introduces auxiliary branches for improved learning. CenterPoint Yin et al. (2021) incorporates an anchor-free detection head. CIA-SSD Zheng et al. (2021) and AFDetV2 Hu et al. (2022) introduce IoU-guided confidence prediction. Additionally, RDIoU Sheng et al. (2022) develops RDIoU-based optimization objectives to address the negative effects of rotation in 3D IoU-based optimization, leading to improved performance. Moreover, methods like 3DSSD Yang et al. (2020) directly perform predictions on raw point locations using PointNet Qi et al. (2017a) feature extraction.

2.2.2 Two-stage 3D object detection from point cloud

Two-stage 3D detectors enhance the performance and robustness of single-stage detectors by incorporating an additional refinement network. Improving the accuracy of 3D object detection is crucial as it directly impacts the security of industrial technical implementations. Generally, these methods can be classified into three categories: semantic information-based refinement (SIR), geometric information-based refinement (GIR), and hybrid information-based refinement (HIR). SIR methods leverage semantic information surrounding the RPN’s predictions. Examples include CenterPoint Yin et al. (2021) using BEV features and Voxel R-CNN Deng et al. (2021) and BtcDet Xu et al. (2022) utilizing multi-level voxel features. These methods divide the 3D proposal into grids and extract semantic features from the RPN’s layers based on the grid locations. GIR methods, on the other hand, focus on refining the 3D proposals using only raw point clouds. LiDAR-RCNN Li et al. (2021) introduces a PointNet-like network to process the points surrounding the proposals, while CT3D Sheng et al. (2021) employs the Transformer architecture for refinement. These methods solely utilize geometric features around the proposals and achieve superior performance compared to those based on multi-level semantic features. Meanwhile, HIR methods combine both proposal-around raw points and multi-level semantic features. Examples include PointRCNN Shi et al. (2019), PV-RCNN Shi et al. (2020a), and PV-RCNN++ Shi et al. (2023). These methods directly concatenate geometric and semantic features, but the performance improvement is limited. In contrast, we propose a novel framework that effectively leverages both SIR and GIR approaches to significantly enhance 3D object detection performance.

2.2.3 3D object detection from point cloud using Transformer

The Transformer Vaswani et al. (2017) has garnered significant attention from researchers in the computer vision field, including applications in classification Touvron et al. (2021); Dosovitskiy et al. (2020) and 2D object detection Carion et al. (2020); Liu et al. (2021c). In the domain of point cloud analysis, several studies have explored the use of Transformers for tasks such as classification, segmentation Zhao et al. (2021); Guo et al. (2021), and 3D object detection Liu et al. (2021d); Mao et al. (2021); Misra et al. (2021); Sheng et al. (2021); He et al. (2022). Group-free Liu et al. (2021d) employs the Transformer to capture interactions among the predictions from the RPN. 3DETR Misra et al. (2021)

treats point clouds as sequential data and produces 3D predictions in a manner similar to DETR Carion et al. (2020). VoTR Mao et al. (2021) incorporates a self-attention scheme into the sparse convolution kernel. CT3D Sheng et al. (2021) adopts an encoder-decoder Transformer architecture as the second-stage refinement module. VoxSet He et al. (2022) models point cloud processing as a set-to-set translation using induced set Transformer Lee et al. (2019), but its performance is limited by the induced latent codes. In this work, we propose an efficient Transformer that combines geometric and semantic features around the 3D proposals. Furthermore, we capitalize on the intrinsic keypoints of the 3D proposals to expedite the convergence rate and enhance the performance of the Transformer network.

3 CT3D: Initial 3D Object Detection Framework with Channel-wise Transformer

Most state-of-the-art methods for 3D object detection follow a two-stage framework that involves 3D region proposal generation and proposal feature refinement. It is worth noting that the popular RPN backbone Yan et al. (2018) achieves a recall rate of over 95% on the KITTI 3D Detection Benchmark, while only achieving 78% Average Precision (AP). This performance gap is attributed to the challenge of encoding objects and extracting robust features from 3D proposals, especially in cases of occlusion or long-range distances. Therefore, effectively modeling geometric relationships among points and leveraging accurate position information during the proposal feature refinement stage is critical for achieving good performance. One important family of models is PointNet Qi et al. (2017a) and its variants Qi et al. (2017b); Pan et al. (2020); Shi et al. (2019), which employ a flexible receptive field to aggregate features based on local regions and permutation-invariant networks. However, these methods suffer from the drawback of incorporating numerous hand-crafted designs, such as neighbor ball radii and grid sizes. Another family of models is voxel-based methods Yan et al. (2018); Song and Xiao (2016); Zheng et al. (2021), which utilize 3D convolutional kernels to extract information from neighboring voxels. However, the performance of such methods is suboptimal due to voxel quantization and sensitivity to hyperparameters. Subsequent studies Zhou and Tuzel (2018); Shi et al. (2020a); Deng et al. (2020); He et al. (2020) have attempted to employ a point-voxel mixed strategy to capture multi-scale features while retaining fine-grained localization, but these approaches are closely tied to specific RPN architectures.

In this section, we provide a brief overview of our initial 3D object detection framework, CT3D Sheng

et al. (2021), illustrated in Figure 2. CT3D is a GIR method that solely utilizes raw points as the feature source for refining the first-stage proposals. Its second-stage network is a channel-wise Transformer, including a raw-point-based embedding, a standard Transformer encoder and a channel-wise decoder.

3.1 Raw-point-based Embedding

The embedding layer is crucial within the Transformer architecture as it transforms input tokens into continuous dense vectors. For point tokens, it is essential to convert the absolute positional coordinates into standardized relative positional coordinates to ensure uniformity. Upon generating proposals via the RPN, we establish a scaled Region of Interest (RoI) within the point clouds corresponding to each proposal. This step aims to compensate for any deviation between the proposal and the corresponding ground-truth box by encompassing as many object points as possible. The scaled RoI area is specifically a cylindrical region with an infinite height and a radius $r = \alpha \sqrt{(\frac{l^c}{2})^2 + (\frac{w^c}{2})^2}$, where α serves as a hyper-parameter, and l and w represent the length and width of the proposal, respectively. Subsequently, we randomly sample $N = 256$ points from within the scaled RoIs, which are denoted as $\mathbf{P} = [\mathbf{p}_1, \dots, \mathbf{p}_N]$, for further processing.

Initially, we compute the relative coordinates between each sampled point and the centroid of the proposal to standardize the input distance feature, represented as $\Delta \mathbf{p}_i^c = \mathbf{p}_i - \mathbf{p}^c$. A straightforward approach is to directly concatenate the proposal information into each point feature, such as $[\Delta \mathbf{p}_i^c, l^c, w^c, h^c, \theta^c, f_i^r]$, where f_i^r represents the raw point feature, such as reflection. However, employing a size-orientation schema for representing the proposal yields only modest improvements in performance. This is attributed to the Transformer encoder’s limited capability to reorient features effectively based on the specified geometric information.

It should be emphasized that keypoints frequently offer a more distinct geometric characteristic in detection tasks Zhou et al. (2019); Law and Deng (2018). To capitalize on this attribute, we introduce an innovative technique termed **keypoints subtraction**, which calculates the relative coordinates between each point and the eight vertices of the associated proposal. These relative coordinates are calculated as $\Delta \mathbf{p}_i^j = \mathbf{p}_i - \mathbf{p}^j$, where $j = 1, \dots, 8$ and \mathbf{p}^j represents the coordinates of the j -th corner point. Notably, the dimensions related to l^c, w^c, h^c , and θ^c are no longer present, as they are embedded within different components of the distance information. This approach allows the newly generated

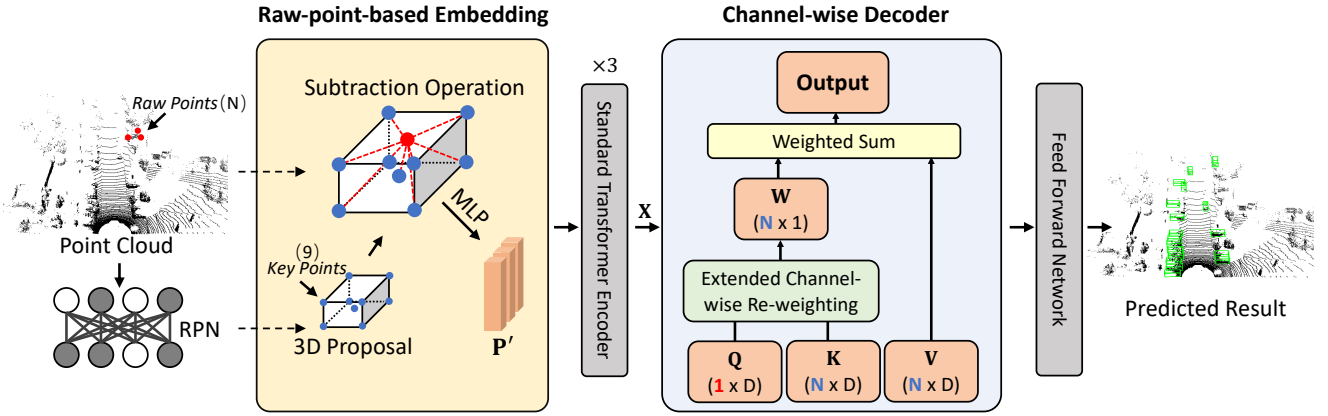


Fig. 2 The overall framework of our proposed CT3D framework. First, our CT3D utilizes an arbitrary RPN to generate coarse 3D proposals. Then, the raw points are gathered and processed using the proposed raw-point-based embedding module. Afterwards, the encoded point features are transformed into an effective proposal feature representation by using three-layer standard Transformer encoder and one novel channel-wise decoder. Here, \mathbf{K} and \mathbf{V} are obtained by linear projection from \mathbf{X} . \mathbf{Q} and \mathbf{W} are learnable parameters.

relative coordinates $\Delta \mathbf{p}_i^j$ to serve as a more informative representation of the proposal. After raw-point-based embedding, the proposal-guided point feature for each sampled point can be expressed as:

$$\mathbf{f}_i = \mathcal{A}([\Delta \mathbf{p}_i^c, \Delta \mathbf{p}_i^1, \dots, \Delta \mathbf{p}_i^8, f_i^r]) \in \mathbb{R}^{N \times D}, \quad (1)$$

where $\mathcal{A}(\cdot)$ is a linear projection layer. To simplify notation, we define $\mathbf{P}' = [\mathbf{f}_i], \forall i$ as the embedded point features.

3.2 Standard Transformer Encoder

The embedded point features are then fed into the Transformer encoder with standard self-attention layers, followed by a feed-forward network (FFN) with residual structure. The self-attention mechanism enables neural networks to concentrate selectively on salient features within a given input context, enhancing the model’s capability for point cloud scene interpretation. By weighting the significance of various input components, the self-attention mechanism facilitates a more nuanced understanding of the spatial relationships inherent in point cloud data. This, in turn, can lead to marked improvements in the network’s performance on tasks requiring detailed contextual awareness. Subsequently, the embedded point features \mathbf{P}' are encoded into \mathbf{X} .

3.3 Channel-wise Decoder

We aim to decode all point features (\mathbf{X}) from the encoder module into a global representation, which is subsequently processed by FFNs for the final detection predictions. Unlike the standard Transformer decoder,

which transforms multiple query embeddings using self-attention and encoder-decoder attention mechanisms, our decoder only operates on a single query embedding based on the following observations: (1). Processing a large number of proposals incurs high memory latency. (2). Transforming multiple query embeddings independently would result in a corresponding number of words or objects, whereas our proposal refinement model requires a single prediction.

Generally, the final proposal representation obtained from the decoder can be seen as a weighted sum of all point features. Our primary objective is to determine dedicated decoding weights for each point. In the following sections, we begin by analyzing the standard cross-attention scheme and subsequently introduce an improved decoding scheme aimed at obtaining more effective decoding weights.

3.3.1 Standard Cross-attention

In the standard Transformer decoder, the conventional cross-attention mechanism employs a learnable vector, known as the query embedding, with a dimension of D to amalgamate point features over all channels. Figure 3(a) provides a graphical illustration of the resultant decoding weight vector for all point features within each attention head. For brevity, we exclude the head index when discussing multi-head attention, with the weight vector being calculated as described:

$$\mathbf{w}^{(s)} = \sigma\left(\frac{\mathbf{q}\mathbf{K}^T}{\sqrt{D}}\right), \quad (2)$$

where \mathbf{K} represents the key embeddings obtained from the encoder output projection, while \mathbf{q} is the corresponding query embedding. Each element of the product $\mathbf{q}\mathbf{K}^T$

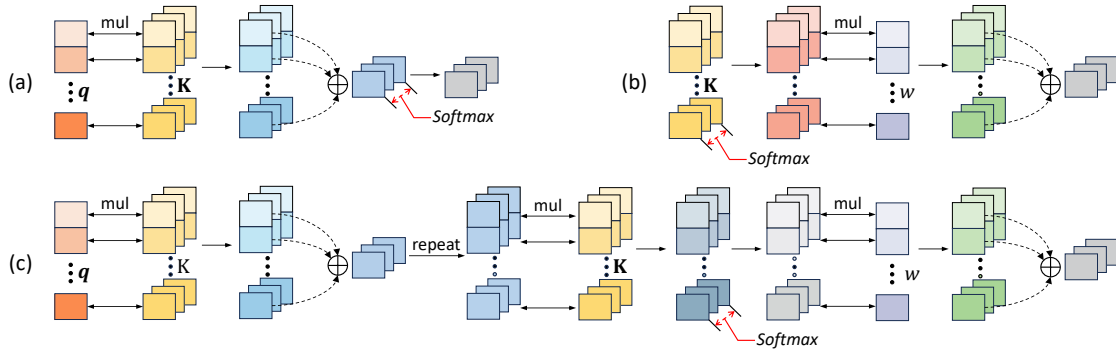


Fig. 3 Illustration of the different decoding schemes: (a) Standard decoding; (b) Channel-wise re-weighting; (c) Extended channel-wise re-weighting.

can be interpreted as a global aggregation for each individual point (i.e., each key embedding). The *softmax* function that follows assigns a decoding weight to each point based on the probability distribution within the normalized vector. However, this process results in decoding weights that are the outcome of a mere global aggregation and they do not account for local channel-specific modeling. Such local modeling is crucial for learning the 3D surface structures of point clouds, as different channels often have significant geometric interdependencies within point cloud data.

3.3.2 Channel-wise Re-weighting

In order to emphasize the channel-wise information for key embeddings \mathbf{K}^T , a straightforward solution is to compute the decoding weight vector for points based on all the channels of \mathbf{K}^T . That is, we generate D different decoding weight vectors for each channel to obtain D decoding values. Further, a linear projection is introduced for these D decoding values to form a united channel-wise decoding vector. As shown in Figure 3(b), this new channel-wise re-weighting for decoding weight vector can be summarized as:

$$\mathbf{w}^{(C)} = \mathbf{s} \cdot \sigma\left(\frac{\mathbf{K}^T}{\sqrt{D}}\right), \quad (3)$$

where \mathbf{s} is a linear projection that compresses D number of decoding values into a re-weighting scalar, $\sigma(\cdot)$ computes the *softmax* along the N dimension. However, the decoding weights computed by $\sigma(\cdot)$ are specific to each channel and do not consider the global aggregation of each point. Consequently, we can infer that the standard cross-attention mechanism in the Transformer decoder emphasizes global aggregation, while the channel-wise re-weighting approach focuses on local aggregation within each channel. To leverage the benefits of both approaches, we introduce an extended channel-wise re-weighting scheme as outlined below.



Fig. 4 The failure case analysis of Voxel R-CNN Deng et al. (2021) and our proposed CT3D. The predicted and ground-truth bounding boxes are shown in green and red, respectively. They generate biased bounding boxes and wrong confidence estimation, respectively. Instead, our newly proposed CT3D++ has good performance on these cases.

3.3.3 Extended Channel-wise Re-weighting

To enhance the channel-wise re-weighting process, we propose a novel extended channel-wise re-weighting scheme. Specifically, we initiate the process by multiplying the query embedding with the key embeddings, allowing the spatial information to be distributed and replicated across all channels. Subsequently, the resulting output is element-wise multiplied with the key embeddings, ensuring the preservation of channel distinctions. This extended channel-wise re-weighting scheme, illustrated in Figure 3(c), generates the following decoding weight vector for all points:

$$\mathbf{w}^{(EC)} = \mathbf{s} \cdot \sigma\left(\frac{\rho(\mathbf{q}\mathbf{K}^T) \odot \mathbf{K}^T}{\sqrt{D}}\right), \quad (4)$$

where $\rho(\cdot)$ is a repeat operator makes $\mathbb{R}^{1 \times N} \rightarrow \mathbb{R}^{D \times N}$. Through this approach, we preserve the global information akin to the channel-wise re-weighting scheme while simultaneously enhancing local and detailed channel interactions beyond what is possible with the standard decoding scheme. Moreover, this extended channel-wise re-weighting only brings 1K+ (Bytes) increase as com-

pared to the other two schemes. As a result, the final decoded proposal representation can be described as follows:

$$\mathbf{y} = \mathbf{w}^{(EC)} \cdot \mathbf{V}, \quad (5)$$

where the value embeddings \mathbf{V} is the linear projection obtained from \mathbf{X} .

3.4 Training Losses

The entire training loss consists of one first-stage RPN loss and one second-stage refinement loss. In the second stage, the detect head loss is a summation of a confidence loss and a regression loss. Following PV-RCNN Shi et al. (2020a), we sample \hat{M} anchors with 1:1 foreground and background ratio, and the confidence targets $\{\hat{u}_i\}_{i=1}^{\hat{M}}$ are the scaled values based on the 3D IoU values $\{o_i\}_{i=1}^{\hat{M}}$ between the 3D proposals and the ground truths. The whole detect head loss can be expressed as:

$$\mathcal{L}_{Re} = \frac{1}{\hat{M}} \left[\sum_{i=1}^{\hat{M}} \mathcal{L}_b(\hat{a}_i, \hat{u}_i) + \mathbf{1}(\hat{z}) \mathcal{L}_r(\hat{b}_i, \hat{v}_i) \right], \quad (6)$$

where \hat{z} represents the condition of $o_i > 0.55$, and \mathcal{L}_b is implemented by binary cross entropy loss. Finally, CT3D is trained by the combination of RPN loss \mathcal{L}_{RPN} and second-stage refinement loss \mathcal{L}_{Re} .

In summary, CT3D represents one of the pioneering works that employ Transformer technology for point cloud-based 3D object detection. It offers improved architectural flexibility and reduced computational costs compared to previous methods in this domain. Nevertheless, there are areas within the CT3D architecture that can be further improved, specifically in terms of second-stage input feature selection and optimizing the high-cost self-attention mechanism.

4 CT3D++: Faster and More Efficient Channel-wise Transformer for 3D Object Detection

Our CT3D method attains cutting-edge performance, surpassing previous methodologies Sheng et al. (2021); however, it encounters limitations in effectively processing large-scale point clouds. This limitation originates from CT3D’s reliance on a GIR framework in its second stage, which can often result in a deficiency of semantic information and consequently, an escalation in false positive predictions. In Figure 4, we compare CT3D with another existing method, Voxel-RCNN, which is an SIR method. The failure cases in Voxel-RCNN often involve biased bounding boxes, whereas the failure cases

in CT3D frequently result in incorrect confidence estimations. Although some existing HIR methods Shi et al. (2019, 2020a, 2023) aim to combine the strengths of both SIR and GIR methods, their performance is often limited by the grid set abstraction operation used for downsampling. Additionally, their RPNs are fixed due to multi-scale voxel feature extraction, which restricts their applicability to real autonomous driving scenarios that typically rely on RPNs without voxel features, such as PointPillar Lang et al. (2019). To the best of our knowledge, there is currently no efficient HIR method that fully exploits the advantages of both SIR and GIR while avoiding these limitations.

To explore a more efficient HIR method, we aim to enhance CT3D by improving its channel-wise Transformer component. The challenge lies in maintaining the flexibility of the overall architecture while effectively incorporating latent space features. It is worth noting that many single-stage approaches for point clouds, such as SECOND Yan et al. (2018), PointPillar Lang et al. (2019), SA-SSD He et al. (2020), CIA-SSD Zheng et al. (2021), and RDIOU Sheng et al. (2022), typically compress point cloud features into a Bird’s Eye View (BEV)-dimensional feature map. This raises the question of **whether we can extend CT3D by incorporating the compressed BEV features into the channel-wise Transformer input.**

Therefore, to ensure scalability, flexibility, and high performance, we investigate the combination of raw point geometric features and BEV semantic features for constructing our refinement network. In Section 5, we present ablation studies to demonstrate the redundancy of multi-scale 3D voxel features in our framework. Specifically, we propose a category-aware raw point sampling strategy to accelerate the sampling process by fixing the capture area for points of the same category. These sampled raw points are then projected into the BEV feature map of the RPN to extract rich semantic information. Moreover, we introduce a lightweight MLP network with only a few hundred units. This MLP network is placed atop the concatenated geometric and semantic features, resulting in a significant enhancement in detection performance. The entire framework of our proposed CT3D++ is visually depicted in Figure 5. In comparison to CT3D, CT3D++ introduces two new modules that can replace their counterparts in CT3D, formed keypoint-induced channel-wise Transformer in the second stage. The first module is the geometric and semantic fusion-based embedding, which efficiently combines geometric and semantic point cloud features as the input for the second-stage Transformer. The second module is the bidirectional point-to-key encoder,

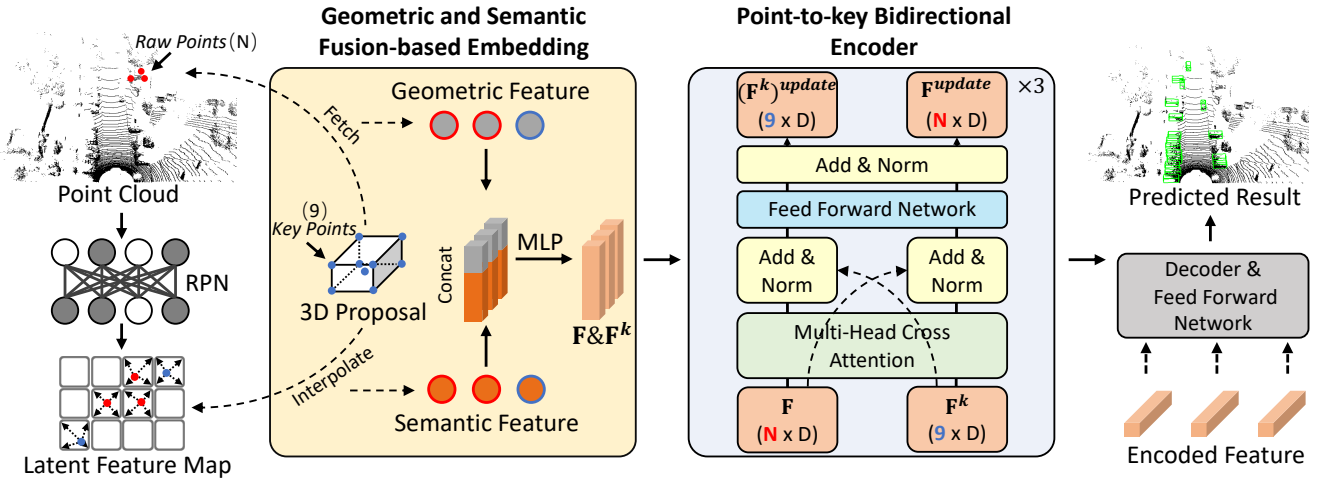


Fig. 5 The overall framework of our proposed CT3D++ framework. First, our CT3D++ utilizes an arbitrary RPN to generate coarse 3D proposals and a latent feature map. Then, the raw points and BEV features are gathered based on the 3D proposals using the proposed geometric and semantic fusion embedding module. After that, an efficient and low-cost point-to-key bidirectional cross-attention scheme is proposed to improve the point features and assign more attention to the foreground points. Finally, the encoded point features are decoded and used to predict the refined 3D object detection results.

which enables more efficient and effective context feature interaction.

4.1 Geometric and Semantic Fusion-based Embedding

We extract the geometric and semantic information from the raw point cloud and BEV feature map, respectively. These two sets of information are then fused and used as the input embedding for the Transformer encoder.

4.1.1 Category-based raw point sampling

We sample the raw points around per bounding box in a cylindrical area with fixed radii according to different categories. This is because the size of the same category in the 3D real-world scene do not vary largely. Note that the point sampling with fixed radii can be accelerated by CUDA parallel processes. Hereinafter, we get N sampled points $\mathbf{P} \in \mathbb{R}^{N \times 3}$ that are directly collected by LiDAR sensor with precise geometric information.

4.1.2 Point-based BEV feature extraction

We project the sampled points \mathbf{P} into the down-sampled BEV feature map, and utilize the bilinear interpolation to get the interpolated features for each point, denoted as \mathbf{T} . The BEV feature map is the last layer of RPN architecture, and thus contains rich semantic information.

4.1.3 Geometric and semantic fusion

For each point, we fuse its geometric and semantic information by applying a simple MLP network $\mathcal{M}(\cdot)$, this process can be expressed as:

$$\mathbf{F} = \mathcal{M}(\mathcal{S}(\mathbf{P}), \mathbf{T}) \in \mathbb{R}^{N \times D}, \quad (7)$$

where $\mathcal{S}(\cdot)$ is an inter-point embedding operation Sheng et al. (2021) that normalizes the point coordinates via 3D coarse bounding boxes and $\mathcal{M}(\cdot)$ projects its input feature into dimension of D . Similarly, we get the fused features of nine key points of per coarse 3D bounding box, and denote it as $\mathbf{F}^k \in \mathbb{R}^{9 \times D}$.

4.2 Point-to-key Bidirectional Encoder

The goal of the attention scheme is to improve the feature representation and assign more attention weights to the foreground points. Its core is to compute the correlation matrix among the inputs. We introduce the **Point-to-Key Bidirectional Cross-Attention (PBC)** as an attention mechanism that outperforms the conventional self-attention scheme Vaswani et al. (2017). Prior to delving into the intricacies of PBC, we shall elucidate the fundamentals of the self-attention mechanism for context.

4.2.1 Self-attention

It is designed to assign different attention weights to the input sequence, such that to enhance the feature

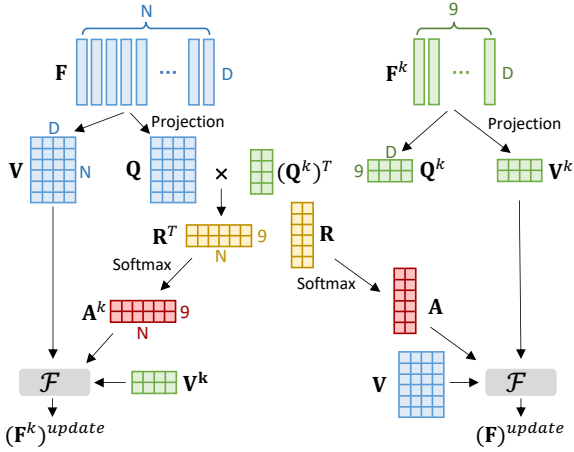


Fig. 6 Illustration of our proposed point-to-key bidirectional cross-attention scheme.

representation of key information while suppress the interference of non-key information. It converts the input into three representations \mathbf{Q} , \mathbf{K} , \mathbf{V} via learnable linear projection, and then computes the attention matrix:

$$\mathbf{A} = \sigma\left(\frac{\mathbf{Q}\mathbf{K}^T}{\sqrt{D}}\right), \quad (8)$$

where $\sigma(\cdot)$ computes the *softmax* along the dimension N . After that, it multiplies attention matrix \mathbf{A} and projected input matrix \mathbf{V} to update the input features:

$$\mathbf{F}^{update} = \mathcal{F}(\mathbf{A} \cdot \mathbf{V} + \mathbf{V}), \quad (9)$$

where $\mathcal{F}(\cdot)$ is a simple feed forward network with residual connection.

Analysis. Enhancement of extracted point cloud features with a self-attention mechanism can substantially improve the representation’s expressiveness and facilitate the modeling of inter-point relational features. However, this approach to feature processing indiscriminately addresses all input points, presenting formidable challenges in terms of convergence when learning the ground truth, as well as in reconciling discrepancies between the ground truth and the 3D proposals. Such convergence issues are especially pronounced in large-scale datasets characterized by substantial variability in the scale and positional information of foreground objects, potentially leading to a marked decline in performance.

4.2.2 Our PBC

Towards the aforementioned convergence issue of the standard self-attention scheme, we propose PBC to enable more simplified and efficient attention-based feature update. A few methods, *e.g.*, Linformer Wang et al. (2020) and clustered attention Vyas et al. (2020) propose

to project the input features into the several clustering centers, however, their performance is limited by the unstable learning process of these clustering centers. In contrast, key points of 3D proposals in our method are inherent clustering points that can be used for complexity reduction. Consequently, we propose *point-to-key bidirectional cross-attention* to replace the self-attention in Transformer encoder as shown in Figure 6. Given the fused features \mathbf{F} and \mathbf{F}^k , we respectively convert them into two separate linear projected features \mathbf{Q} , \mathbf{V} and \mathbf{Q}^k , \mathbf{V}^k . We first compute the correlation matrix based on \mathbf{Q} and \mathbf{Q}^k as:

$$\mathbf{R} = \mathbf{Q} \cdot (\mathbf{Q}^k)^T. \quad (10)$$

Then, we can obtain the bidirectional attention matrices that respectively represent the assigned attention values for raw points and key points by computing:

$$\mathbf{A} = \sigma\left(\frac{\mathbf{R}}{\sqrt{D}}\right), \quad \mathbf{A}^k = \hat{\sigma}\left(\frac{\mathbf{R}^T}{\sqrt{D}}\right), \quad (11)$$

where $\hat{\sigma}$ computes the *softmax* along the dimension 9. Both the sampled point features and the key point features are updated by their corresponding bidirectional attention matrices. After applying the attention-based aggregation for the input features, we adopt a simple FFN $\mathcal{F}(\cdot)$ with residual connection, yielding:

$$\mathbf{F}^{update} = \mathcal{F}(\mathbf{A} \cdot \mathbf{V}^k + \mathbf{V}), \quad (12)$$

$$(\mathbf{F}^k)^{update} = \mathcal{F}(\mathbf{A}^k \cdot \mathbf{V} + \mathbf{V}^k). \quad (13)$$

The above encoder layer can be repeated and stacked into a deep encoder module. We empirically find that three encoder layers give a good performance. The encoder module mutually refines the features of the sampled points and the key points. Subsequently, the outputs of the encoder module are fed into a Transformer decoder to generate a global representation.

4.3 Channel-wise Decoder and Training Losses

After obtaining the enhanced point features through the PBC scheme, it is necessary to aggregate them into a single global feature representation. To accomplish this, we employ the channel-wise decoder mentioned in Section 3.3 to summarize the point features, represented as $\mathbf{F}^{update} \in \mathbb{R}^{N \times D}$, into a compact form denoted as $\mathbf{F}^{dec} \in \mathbb{R}^{1 \times D}$. Subsequently, two FFNs are utilized to generate the final regression residuals and confidence estimation. The final confidence score is derived by averaging the outputs from both the RPN and the second-stage estimations. Noting that CT3D++ employs the same training loss approach as that of CT3D.

5 Experiments

In this section, we provide exhaustive experimental settings and implementation details for both the CT3D and CT3D++ frameworks. Subsequently, we compare our proposed CT3D and CT3D++ methods with state-of-the-art point cloud-based 3D object detection approaches. Finally, we conduct comprehensive ablation studies to assess the effectiveness of each component in both CT3D and CT3D++ methods.

5.1 Datasets and Evaluation Metrics

5.1.1 Waymo Open Dataset

It collects 798 training and 202 validation sequences, where there are 158,361 LiDAR samples and 40,077 LiDAR samples, respectively. It has a much larger perception area supported by 5 LiDAR sensors as compared to the perception area of KITTI with only 1 LiDAR sensor. Currently, it is the largest outdoor 3D object detection dataset for autonomous driving. In main results, we report AP and average precision by heading (APH) performance on *Vehicle* category with IoU larger than 0.7 for 3D/BEV detection. Moreover, performance on different distances (*i.e.*, 0-30m, 30-50m and 50m-*Inf*) are separately exhibited, and two detection difficulty levels (*i.e.*, LEVEL_1 with more than 5 points and LEVEL_2 with no more than 5 points). In ablation studies, we also report *Cyclist* results with IoU larger than 0.5.

5.1.2 KITTI

It is a classical outdoor 3D object detection dataset for autonomous driving. It collects 7,481 frames of point cloud data for training and another 7,518 frames of point cloud data for testing. Following the common setting as in Yan et al. (2018); Lang et al. (2019); Shi et al. (2020a); Sheng et al. (2021), we split the whole training data into *train* set with 3,712 samples and *val* set with 3,769 samples for experimental studies. We report the AP values for *car* category with IoU larger than 0.7. In addition, we report *Pedestrian* and *Cyclist* categories with IoU larger than 0.5. Moreover, the results on three difficulty levels *i.e.*, *easy*, *moderate* and *hard*, are exhibited according to the occlusion, truncation, and the number of corresponding image pixels of objects.

5.2 Implementation Details

As shown in previous works Yan et al. (2018); Shi et al. (2020a); Deng et al. (2021), the implementation details

for Waymo Open Dataset and KITTI are quite similar, and the major difference lies in the different sizes of perception area per frame. Our implementation mainly follows these previous works. The default RPN consists of one 3D backbone and one 2D backbone. For the voxel size and XYZ ranges, we adopt the default setting in OpenPCDet Team (2020). The default 2D backbone contains two blocks, the first block is implemented by 5 CNN layers for KITTI and 6 CNN layers for Waymo Open Dataset to keep the same resolution with the output of 3D backbone. The second block is implemented by 1 CNN layer and 4 Transformer layers (using the setting of $4\times$ expansion in FFN layers and 4 attention heads) with half the resolution. Finally, one fractionally-strided convolution layer is adopted to double the resolution. For KITTI, the default 3D backbone network is implemented by four-stage sparse convolution, and the filter numbers are 16, 32, 48, and 64, respectively. The fixed perception radius is 2.6m for *car*, and 1.2m for both *pedestrian* and *cyclist*. For Waymo Open Dataset, the corresponding filter numbers are 16, 32, 64, and 128, respectively. The default 2D backbone network is composed of 2d CNN and Swin-Transformer Liu et al. (2021c) layers. For CT3D, we set the perception radius scaling parameters $\alpha = 1.2$. In object-based raw point sampling, we set $N = 256$. For CT3D++, the fixed perception radius is 3.1m, 1.3m for *vehicle*, *pedestrian/cyclist*, respectively. In category-based raw point sampling, we set $N = 255$. For both object-based and category-based raw point sampling strategies, we pad the sampled points with the first point if the number of points within the perception area is less than 255.

5.2.1 Training and Inference

All models are end-to-end trained from scratch. We use 8 V100 GPUs with batch size 24 for KITTI and batch size 16 for Waymo Open Dataset. CT3D’s learning rate is $1e-3$, while CT3D++ uses $5e-4$. In training, 64 positive proposals are selected for regression and, with 64 negative samples, for confidence estimation. During inference, the top 100 3D proposals by classification score undergo further regression refinement and confidence evaluation.

5.3 Comparison Results on Waymo

We train our model on the entire Waymo training set and evaluate its performance on the Waymo validation set, as presented in Table 1. Our CT3D++ method outperforms previous state-of-the-art works, such as RDIOU Sheng et al. (2022), BtcDet Xu et al. (2022), and PV-RCNN++ Shi et al. (2023), in both 3D and BEV

Table 1 Performance comparisons with state-of-the-art methods on the validation set of Waymo Open Dataset for vehicle detection.

Method	3D AP/APH (IoU=0.7)				BEV AP/APH (IoU=0.7)			
	Overall	0-30m	30-50m	50m-Inf	Overall	0-30m	30-50m	50m-Inf
LEVEL_1								
PV-RCNN Shi et al. (2020a)	70.3/69.7	91.9/91.3	69.2/68.5	42.2/41.3	80.0/82.1	97.4/96.7	83.0/82.0	65.0/63.2
Voxel-RCNN Deng et al. (2021)	75.6/-	92.5/-	74.1/-	53.2/-	88.2/-	97.6/-	87.3/-	77.7/-
LiDAR-RCNN Li et al. (2021)	76.0/75.5	92.1/91.6	74.6/74.1	54.5/53.4	90.1/89.3	97.0/96.5	89.5/88.6	78.9/77.4
CenterPoint Yin et al. (2021)	76.7/76.2	-	-	-	-	-	-	-
VoTr-TSD Mao et al. (2021)	75.0/74.3	92.3/91.7	73.4/72.6	51.1/50.0	-	-	-	-
VoxelSet He et al. (2022)	77.8/-	92.8/-	77.2/-	54.4/-	90.3/-	96.1/-	88.1/-	78.0/-
RDIOU Sheng et al. (2022)	78.4/78.0	93.0/92.6	75.4/74.9	56.2/55.6	91.6/91.0	98.1/97.7	90.8/90.2	82.4/81.1
IA-SSD Zhang et al. (2022)	70.5/69.7	-	-	-	-	-	-	-
BtcDet Xu et al. (2022)	78.6/78.1	96.1/-	77.6/-	54.5/-	-	-	-	-
AFDetV2 Hu et al. (2022)	77.6/77.1	-	-	-	-	-	-	-
PV-RCNN++ Shi et al. (2023)	79.3/78.8	-	-	-	-	-	-	-
LargeKernel3D Chen et al. (2023)	78.1/77.6	-	-	-	-	-	-	-
CT3D	76.3/75.8	92.5/92.0	75.1/74.6	55.4/54.5	90.5/90.0	97.6/97.0	88.1/87.1	78.9/77.4
CT3D++	80.5/79.9	93.7/93.2	79.3/78.8	60.0/59.3	92.2/91.5	98.2/97.8	91.3/90.7	83.6/82.4
LEVEL_2								
PV-RCNN Shi et al. (2020a)	65.4/64.8	91.6/91.0	65.1/64.5	36.5/35.7	77.5/76.6	94.6/94.0	80.4/79.4	55.4/53.8
Voxel-RCNN Deng et al. (2021)	66.6/-	91.7/-	67.9/-	40.8/-	81.1/-	97.0/-	81.4/-	63.3/-
LiDAR-RCNN Li et al. (2021)	68.3/67.9	91.3/90.9	68.5/68.0	42.4/41.8	81.7/81.0	94.3/93.9	82.3/81.5	65.8/64.5
CenterPoint Yin et al. (2021)	68.8/68.3	-	-	-	-	-	-	-
VoTr-TSD Mao et al. (2021)	65.9/65.3	-	-	-	-	-	-	-
VoxelSet He et al. (2022)	70.21/-	92.05/-	70.10/-	43.20/-	80.56/-	96.79/-	80.44/-	62.37/-
RDIOU Sheng et al. (2022)	69.5/69.1	92.3/91.9	69.3/68.9	43.7/43.1	83.1/82.5	97.5/97.1	85.2/84.6	68.3/67.2
BtcDet Xu et al. (2022)	70.1/69.6	96.0/-	70.1/-	43.9/-	-	-	-	-
IA-SSD Zhang et al. (2022)	61.6/60.8	-	-	-	-	-	-	-
PV-RCNN++ Shi et al. (2023)	70.6/70.2	-	-	-	-	-	-	-
LargeKernel3D Chen et al. (2023)	69.8/69.4	-	-	-	-	-	-	-
CT3D	69.1/68.6	91.8/91.2	68.9/68.4	42.6/42.0	81.7/81.2	97.1/96.6	82.2/81.5	64.3/63.4
CT3D++	71.5/71.0	93.0/92.5	73.3/72.8	48.1/47.5	85.7/85.0	97.7/97.3	85.7/85.1	69.7/68.5

Table 2 Comparison with the state-of-the-art methods on the KITTI *test* benchmark for *car* detection.

Method	Car-3D (IoU=0.7)				Car-BEV (IoU=0.7)			
	mAP	Easy	Moderate	Hard	mAP	Easy	Moderate	Hard
SA-SSD He et al. (2020)	80.90	88.75	79.79	74.16	90.67	95.03	91.03	85.96
PV-RCNN Shi et al. (2020a)	82.83	90.25	81.43	76.82	90.59	94.98	90.65	86.14
Voxel R-CNN Deng et al. (2021)	83.19	90.90	81.62	77.06	89.94	94.85	88.83	86.13
LiDAR-RCNN Li et al. (2021)	76.45	85.97	74.21	69.18	-	-	-	-
VoTR-TSD Mao et al. (2021)	83.71	89.90	82.09	79.14	90.17	94.03	90.34	86.14
VoxSeT He et al. (2022)	82.68	88.53	82.06	77.46	89.35	92.70	89.07	86.29
RDIOU Sheng et al. (2022)	83.40	90.65	82.30	77.26	89.77	94.90	89.75	84.67
BtcDet Xu et al. (2022)	83.86	90.64	82.86	78.09	88.90	92.81	89.34	84.55
IA-SSD Zhang et al. (2022)	81.17	88.34	80.13	75.04	88.82	92.79	89.33	84.35
PV-RCNN++ Shi et al. (2023)	83.06	90.14	81.88	77.15	89.12	92.66	88.74	85.97
CT3D	82.25	87.83	81.77	77.16	88.42	92.36	88.83	84.07
CT3D++	84.25	90.91	82.44	79.41	91.66	95.12	91.35	88.50

detection tasks, achieving remarkable performance gains. Specifically, our proposed method achieves a significant improvement of +1.9%, +1.4%, and +0.8% in terms of APH of LEVEL_2 difficulty for 3D detection, which is the most important metric for Waymo Open Dataset, compared to RDIOU, BtcDet, and PV-RCNN++, respectively. Moreover, for BEV detection, our CT3D++ surpasses all other methods in all distance ranges and difficulty levels by large margins. Notably, our method

brings more improvement for objects with distances greater than 30m, which often suffer from occlusion and signal miss problems and thus require semantic information. As compared to our previous proposed method CT3D, CT3D++ surpasses it with 2.4%APH. In conclusion, our consistent performance improvements on the largest point cloud-based 3D object detection dataset demonstrate the effectiveness of our proposed CT3D++ method.

Table 3 Performance comparisons with state-of-the-art methods on the KITTI *val* set with 11 recall positions. All models reported here are trained with all the three categories.

Method	Car-3D (IoU=0.7)				Ped.-3D (IoU=0.5)				Cyc.-3D (IoU=0.5)			
	mAP	Easy	Moderate	Hard	mAP	Easy	Moderate	Hard	mAP	Easy	Moderate	Hard
VoxelNet Zhou and Tuzel (2018)	70.09	81.97	65.46	62.85	53.38	57.86	53.42	48.87	53.31	67.17	47.65	45.11
SECOND Yan et al. (2018)	81.48	88.61	78.62	77.22	52.42	56.55	52.98	47.73	70.29	80.59	67.16	63.11
PointPillar Lang et al. (2019)	79.46	86.46	77.28	74.65	52.65	57.75	52.29	47.91	67.49	80.06	62.69	59.71
3DSSD Yang et al. (2020)	82.61	89.71	79.45	78.67	-	-	-	-	-	-	-	-
Part-A ² Shi et al. (2020b)	82.60	89.56	79.41	78.84	60.40	65.69	60.05	55.45	73.63	85.50	69.90	65.49
PV-RCNN Shi et al. (2020a)	83.91	89.35	83.69	78.70	56.58	63.12	54.84	51.78	73.35	86.06	69.48	64.50
RDIOU Sheng et al. (2022)	84.27	89.16	85.24	78.41	57.75	63.26	57.47	52.53	71.78	83.32	68.39	63.63
CT3D	84.30	89.11	85.04	78.76	59.94	64.23	59.84	55.76	74.93	85.04	71.71	68.05
CT3D++	86.77	89.53	85.28	85.51	63.06	67.89	63.24	58.04	75.55	86.33	72.45	67.87

5.4 Comparison Results on KITTI

We train the model on all the KITTI training data (*i.e.*, *trainval* set), and report the *car* category detection performance of our method on KITTI *test* benchmark. The comparison results with the state-of-the-art methods are listed in Table 2. Our proposed CT3D++ method ranks in the 1st place over almost all the metrics with significant improvement. Specifically, we achieve 90.91%, 82.44% and 79.41% AP on 3D detection for *car* category with 84.25% mean average precision (mAP). Our method outperforms the most recent work RDIOU Sheng et al. (2021), BtcDet Xu et al. (2022) with +0.85% and +0.39% improvement, respectively, on 3D detection. Additionally, our method surpasses RDIOU and BtcDet with +1.89% and +2.76% improvement, respectively, on BEV detection, which is also an important task when evaluating on KITTI *test* benchmark Geiger et al. (2013).

In addition, we also provide the comparisons with state-of-the-art methods in terms of three categories on KITTI *val* set in Table 3. Unlike many related works Deng et al. (2021); He et al. (2020); Mao et al. (2021) that only train models on *car* category or train different models for different categories Xu et al. (2022), our proposed CT3D++ conducts multi-class training and still can achieve promising performance. Particularly, our CT3D++ leads a large margin as compared to the second-best method CT3D Sheng et al. (2021). For *car* detection, we can outperform the current best performance with +2.47% on mAP. Especially, our CT3D++ significantly improves the detection performance on *pedestrian* and *cyclist* categories, leading to +2.66% and +0.62% improvements on mAP, respectively, compared with the second-best performance. To sum up, our CT3D++ performs significantly better than state-of-the-art methods over almost all categories and all difficulty levels. There only exists tiny performance drop on *easy*-level *car* detection and *hard*-level *cyclist* detec-

tion. These strong results further verify the effectiveness of our method.

5.5 Ablation Study

We conduct extensive experiments to analyze the effects of major contributions in our method. All models are trained on 20% Waymo *train* set like PV-RCNN++ Shi et al. (2023) and evaluated on full Waymo *val* set. During training, we fix the RPN parameters for fare comparisons and train the second-stage refinement network with the fixed learning rate (*i.e.*, $5e-4$), training epochs (*i.e.*, 16) and batch size (*i.e.*, 24). We report the performance of *Vehicle* and *Cyclist* detection on APH metric with LEVEL_1 and LEVEL_2, respectively.

5.5.1 Effects on different RPNs

To demonstrate the flexibility of our CT3D++ framework, we conduct experiments using two different RPNs: PointPillar Lang et al. (2019) and CT-stacked Sheng et al. (2022). The results, reported in Table 4, illustrate that our method consistently outperforms both RPNs with significant margins across all evaluation metrics.

5.5.2 Effects on channel-wise decoder

Table 5 demonstrates that the extended channel-wise re-weighting significantly outperforms both the standard cross-attention and channel-wise re-weighting approaches. This substantial improvement can be attributed to the integration of standard decoding and channel-wise re-weighting techniques, which enables more effective decoding weights through global and channel-wise local aggregation.

5.5.3 Effects on different refinement networks

We compare with four other refinement methods, including one SIR, one GIR, and two HIR approaches. To en-

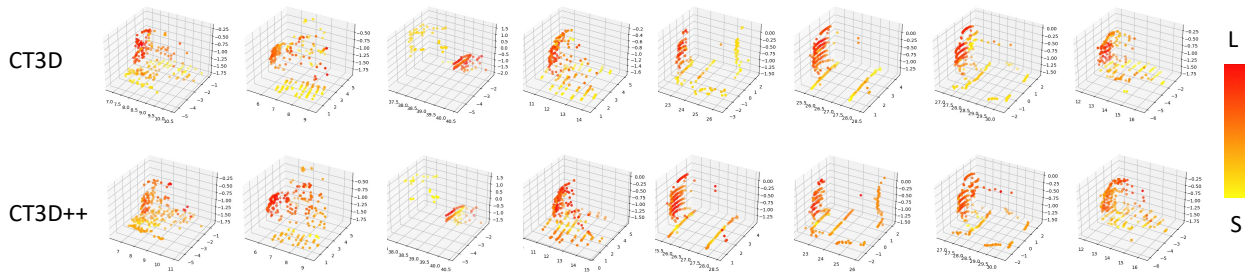


Fig. 7 Attention maps of several instances generated by encoder of CT3D and CT3D++, respectively.

Table 4 Ablation study on different RPNs.

Method	Vehicle		Cyclist	
	L_1	L_2	L_1	L_2
PointPillar Lang et al. (2019)	69.7	61.5	51.8	49.9
CT3D (PointPillar)	70.2	62.6	54.4	52.3
CT3D++ (PointPillar)	73.8	64.8	58.5	56.2
CT-stacked Sheng et al. (2022)	74.3	65.4	54.4	52.6
CT3D (CT-stacked)	75.1	66.7	57.9	55.7
CT3D++ (CT-stacked)	76.3	68.9	63.6	61.1

Table 5 Ablation study on channel-wise decoder.

Method	Vehicle		Cyclist	
	L_1	L_2	L_1	L_2
Standard cross-attention	73.9	65.2	55.5	53.5
Channel-wise re-weighting	73.9	65.3	55.5	53.6
Extended channel-wise re-weighting	76.3	68.9	63.6	61.1

Table 6 Ablation study on different refinement networks. We reproduce (I): Voxel R-CNN Deng et al. (2021) (III): PV-RCNN Shi et al. (2020a) and (IV): PV-RCNN++ Shi et al. (2023) with same RPN. (IV): CT3D (V): CT3D++ Time is tested by 1 V100 GPU with batch size 1.

Method	Refine	Time (ms)	Vehicle		Cyclist	
			L_1	L_2	L_1	L_2
Voxel R-CNN	SIR	85.6	74.3	65.5	62.0	59.6
PV-RCNN	HIR	367.5	73.9	65.1	56.9	54.9
PV-RCNN++	HIR	225.9	75.2	67.5	61.0	58.7
CT3D	GIR	178.6	73.0	64.3	55.1	53.0
CT3D++	HIR	146.2	76.3	68.9	63.6	61.1

sure a fair comparison, we use the same fixed-parameter RPN for all four methods, namely Voxel R-CNN Deng et al. (2021), CT3D Sheng et al. (2021), PV-RCNN Shi et al. (2020a), and PV-RCNN++ Shi et al. (2023). The results are presented in Table 6, showing that our method significantly outperforms all the other methods. We attribute our success to the fusion of geometric and semantic information, which is absent in Voxel R-CNN and CT3D. Although PV-RCNN and PV-RCNN++ are also HIR methods that integrate both types of infor-

Table 7 Ablation study on the geometric and semantic fusion embedding. Vox. means incorporating voxel features extracted from the middle layers of RPN.

Geo.	Sem.	Vox.	Vehicle		Cyclist	
			L_1	L_2	L_1	L_2
✓			76.1	68.2	63.4	60.5
	✓		73.0	64.1	53.8	51.9
✓	✓		76.3	69.0	63.6	61.1
✓	✓	✓	76.3	68.9	63.6	61.1

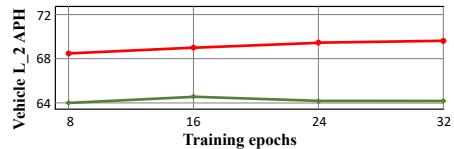


Fig. 8 Performance comparison of self-attention and our proposed PBC schemes using Vehicle LEVEL_2 APH metric.

Table 8 Ablation study on our proposed PBC scheme.

Encoding scheme	Time (ms)	Vehicle		Cyclist	
		L_1	L_2	L_1	L_2
MLP	1.3	75.4	66.4	62.7	60.2
Self-attention	23.9	73.4	64.5	55.3	53.6
PBC	16.6	76.3	68.9	63.6	61.1

Table 9 Ablation study on different kinds of decoding points.

Decoding on	Vehicle		Cyclist	
	L_1	L_2	L_1	L_2
Key points	76.0	68.6	62.9	60.4
Raw points	76.3	68.9	63.6	61.1

mation, their performance falls short of ours, further demonstrating the efficacy of our fusion-based refinement network. Regarding latency, our CT3D++ requires only 146.2ms per frame when run on a single V100 GPU, while achieving significantly improved performance as compared to CT3D Sheng et al. (2021), PV-RCNN Shi et al. (2020a) and PV-RCNN++ Shi et al. (2023) with much less time required.

Table 10 Ablation study on the different sampling strategies. Time is tested with 1 V100 GPU and batch size 4.

Sampling	Time (ms)	Vehicle		Cyclist	
		L_1	L_2	L_1	L_2
Object-based	111.4	76.4	69.0	63.8	61.2
Category-based	60.5	76.3	68.9	63.6	61.1

Table 11 Comparisons between the standard self-attention and our proposed PBC schemes with different training epochs. The performance of the last epoch is reported.

Encoding scheme	Training epochs	Vehicle		Cyclist	
		L_1	L_2	L_1	L_2
Self-attention	8	72.8	64.0	54.3	52.4
PBC	8	75.9	68.5	62.8	60.2
Self-attention	16	73.4	64.5	55.3	53.6
PBC	16	76.3	68.9	63.6	61.1
Self-attention	24	72.9	64.1	55.6	53.6
PBC	24	76.7	69.3	64.5	62.3
Self-attention	32	72.9	64.1	55.7	53.5
PBC	32	78.5	69.4	64.8	62.6

5.5.4 Effects on geometric and semantic fusion embedding

We evaluate the effectiveness of this module by adding different features from RPN, as shown in Table 7. The results demonstrate that the combination of geometric features (*i.e.*, raw points) and semantic features (*i.e.*, BEV feature map) leads to significant performance improvements. We also test adding voxel features from the middle layers of RPN, similar to Voxel R-CNN Deng et al. (2021), and observe no significant improvement. This confirms that the semantic information provided by BEV features is sufficient.

5.5.5 Effects on the PBC scheme

We compare our proposed scheme with other feature enhancement techniques, such as the MLP and self-attention Vaswani et al. (2017) in Table 8. Our PBC scheme exhibits significant better performance than both the MLP and self-attention schemes. This is because the self-attention scheme is highly complex and difficult to converge, while the capabilities of MLP networks are limited. The self-attention scheme is highly complex and difficult to converge, as evidenced by its poorer performance compared to the simple MLP, as shown in the 1st and 2nd rows of the table. In contrast, our PBC scheme explicitly models the relationship between the raw points and key points, making it more efficient in estimating residuals and confidence. Moreover, our PBC scheme achieves a 31.3% reduction in runtime compared

to the self-attention scheme, while still significantly improving 3D detection performance. This indicates that our method is highly efficient. Additionally, in Figure 7, we visualize the attention maps of several instances generated by our PBC scheme, which clearly shows that the network assigns more attention (red) to foreground points and less attention (yellow) to background points.

5.5.6 Effects on the different kinds of decoding points

Table 9 shows the results of experiments conducted to investigate the influence of different kinds of decoding points (*i.e.*, 255 sampled raw points vs. 9 key points). While there is information exchange between the raw point features and key point features, the results show that decoding with raw points outperforms key points-based decoding.

5.5.7 Effects on the category-based raw point sampling

Table 10 compares our category-based raw point sampling strategy with object-based raw point sampling. The results indicate that category-based raw point sampling can significantly increase the training/inference speed while only causing a slight performance drop compared to object-based raw point sampling. These results demonstrate that our method is not highly sensitive to the sampled range and can maintain robustness to incomplete point clouds.

5.5.8 More comparisons between PBC and self-attention

Table 11 presents additional experiments conducted to validate the effectiveness of our proposed PBC scheme. The findings indicate that our method attains accelerated convergence and superior performance relative to the conventional self-attention framework, thereby furnishing additional corroboration of the efficacy of our PBC scheme. In addition, we plot the corresponding line chart of *Vehicle* LEVEL.2 APH in Figure 8, which clearly shows that our PBC scheme outperforms the standard self-attention scheme in terms of convergence and performance.

6 Conclusion

In this paper, we have presented two innovative frameworks, CT3D and CT3D++, which significantly advance the state-of-the-art in 3D object detection from point clouds. Our work is predicated on the idea that the key to improving detection performance lies in minimal hand-crafted design and in leveraging the strengths

of Transformers for feature encoding. CT3D lays the foundation by introducing a raw-point-based embedding process followed by a standard Transformer encoder and a channel-wise decoder, which together enhance the process of feature extraction from point clouds. Building upon the success of CT3D, we developed CT3D++, which further refines the detection process through the integration of geometric and semantic information. This is achieved by a geometric and semantic fusion-based embedding technique that enriches proposal-aware features with more meaningful context. Moreover, the innovative point-to-key bidirectional encoder implemented in CT3D++ not only improves feature representation but also reduces computational overhead, making it a more efficient and practical solution for real-world applications. Our experimental results demonstrate that both CT3D and CT3D++ achieve superior performance on benchmark datasets like KITTI and Waymo Open Dataset, confirming the effectiveness of our approaches in handling the complexity and variability of real-world 3D environments. The scalability and adaptability of our frameworks make them suitable for a wide array of applications in autonomous driving, robotics, and beyond.

References

- Yuanzhouhan Cao, Zifeng Wu, and Chunhua Shen. Estimating depth from monocular images as classification using deep fully convolutional residual networks. *IEEE Transactions on Circuits and Systems for Video Technology (TCSVT)*, 28(11):3174–3182, 2017. [3](#)
- Nicolas Carion, Francisco Massa, Gabriel Synnaeve, Nicolas Usunier, Alexander Kirillov, and Sergey Zagoruyko. End-to-end object detection with transformers. In *Proceedings of the European Conference on Computer Vision*, pages 213–229. Springer, 2020. [3](#), [4](#), [5](#)
- Yuning Chai, Pei Sun, Jiquan Ngiam, Weiyue Wang, Benjamin Caine, Vijay Vasudevan, Xiao Zhang, and Dragomir Anguelov. To the point: Efficient 3d object detection in the range image with graph convolution kernels. In *Proceedings of the IEEE/CVF Conference on Computer Vision and Pattern Recognition*, pages 16000–16009, 2021. [4](#)
- Shu Chen, Zhengdong Pu, Xiang Fan, and Beiji Zou. Fixing defect of photometric loss for self-supervised monocular depth estimation. *IEEE Transactions on Circuits and Systems for Video Technology (TCSVT)*, 32(3):1328–1338, 2021. [3](#)
- Xiaozhi Chen, Huimin Ma, Ji Wan, Bo Li, and Tian Xia. Multi-view 3d object detection network for autonomous driving. In *Proceedings of the IEEE Conference on Computer Vision and Pattern Recognition (CVPR)*, pages 1907–1915, 2017. [4](#)
- Yongjian Chen, Lei Tai, Kai Sun, and Mingyang Li. Monopair: Monocular 3d object detection using pairwise spatial relationships. In *Proceedings of the IEEE/CVF Conference on Computer Vision and Pattern Recognition (CVPR)*, pages 12093–12102, 2020. [3](#)
- Yukang Chen, Jianhui Liu, Xiangyu Zhang, Xiaojuan Qi, and Jiaya Jia. Largekernel3d: Scaling up kernels in 3d sparse cnns. In *Proceedings of the IEEE/CVF Conference on Computer Vision and Pattern Recognition*, pages 13488–13498, 2023. [12](#)
- Jiajun Deng, Shaoshuai Shi, Peiwei Li, Wengang Zhou, Yanyong Zhang, and Houqiang Li. Voxel r-cnn: Towards high performance voxel-based 3d object detection. *arXiv preprint arXiv:2012.15712*, 2020. [5](#)
- Jiajun Deng, Shaoshuai Shi, Peiwei Li, Wengang Zhou, Yanyong Zhang, and Houqiang Li. Voxel r-cnn: Towards high performance voxel-based 3d object detection. *Proceedings of the AAAI Conference on Artificial Intelligence*, 35(2): 1201–1209, 2021. [1](#), [2](#), [4](#), [7](#), [11](#), [12](#), [13](#), [14](#), [15](#)
- Mingyu Ding, Yuqi Huo, Hongwei Yi, Zhe Wang, Jianping Shi, Zhiwu Lu, and Ping Luo. Learning depth-guided convolutions for monocular 3d object detection. In *Proceedings of the IEEE/CVF Conference on Computer Vision and Pattern Recognition Workshops*, pages 1000–1001, 2020. [3](#)
- Alexey Dosovitskiy, Lucas Beyer, Alexander Kolesnikov, Dirk Weissenborn, Xiaohua Zhai, Thomas Unterthiner, Mostafa Dehghani, Matthias Minderer, Georg Heigold, Sylvain Gelly, et al. An image is worth 16x16 words: Transformers for image recognition at scale. *arXiv preprint arXiv:2010.11929*, 2020. [4](#)
- Lue Fan, Xuan Xiong, Feng Wang, Naiyan Wang, and Zhaoxiang Zhang. Rangedet: In defense of range view for lidar-based 3d object detection. In *Proceedings of the IEEE/CVF International Conference on Computer Vision*, pages 2918–2927, 2021. [4](#)
- Andreas Geiger, Philip Lenz, Christoph Stiller, and Raquel Urtasun. Vision meets robotics: The kitti dataset. *The*

- International Journal of Robotics Research*, 32(11):1231–1237, 2013. 13
- Meng-Hao Guo, Jun-Xiong Cai, Zheng-Ning Liu, Tai-Jiang Mu, Ralph R Martin, and Shi-Min Hu. Pct: Point cloud transformer. *Computational Visual Media*, 7(2):187–199, 2021. 4
- Chenhong He, Hui Zeng, Jianqiang Huang, Xian-Sheng Hua, and Lei Zhang. Structure aware single-stage 3d object detection from point cloud. In *Proceedings of the IEEE Conference on Computer Vision and Pattern Recognition (CVPR)*, pages 11873–11882, 2020. 1, 4, 5, 8, 12, 13
- Chenhong He, Ruihuang Li, Shuai Li, and Lei Zhang. Voxel set transformer: A set-to-set approach to 3d object detection from point clouds. In *Proceedings of the IEEE/CVF Conference on Computer Vision and Pattern Recognition*, pages 8417–8427, 2022. 1, 4, 5, 12
- Yihan Hu, Zhuangzhuang Ding, Runzhou Ge, Wenxin Shao, Li Huang, Kun Li, and Qiang Liu. Afdetv2: Rethinking the necessity of the second stage for object detection from point clouds. *Proceedings of the AAAI Conference on Artificial Intelligence*, 36(1):969–979, 2022. 4, 12
- Junjie Huang and Guan Huang. Bevdet4d: Exploit temporal cues in multi-camera 3d object detection. *arXiv preprint arXiv:2203.17054*, 2022. 3
- Junjie Huang, Guan Huang, Zheng Zhu, Yun Ye, and Dalong Du. Bevdet: High-performance multi-camera 3d object detection in bird-eye-view. *arXiv preprint arXiv:2112.11790*, 2021. 3
- Jason Ku, Melissa Mozifian, Jungwook Lee, Ali Harakeh, and Steven L Waslander. Joint 3d proposal generation and object detection from view aggregation. In *2018 IEEE/RSJ International Conference on Intelligent Robots and Systems (IROS)*, pages 1–8, 2018. 4
- Alex H Lang, Sourabh Vora, Holger Caesar, Lubing Zhou, Jiong Yang, and Oscar Beijbom. Pointpillars: Fast encoders for object detection from point clouds. In *Proceedings of the IEEE/CVF Conference on Computer Vision and Pattern Recognition (CVPR)*, pages 12697–12705, 2019. 1, 4, 8, 11, 13, 14
- Hei Law and Jia Deng. Cornernet: Detecting objects as paired keypoints. In *Proceedings of the European Conference on Computer Vision (ECCV)*, pages 734–750, 2018. 5
- Juho Lee, Yoonho Lee, Jungtaek Kim, Adam Kosior, Seungjin Choi, and Yee Whye Teh. Set transformer: A framework for attention-based permutation-invariant neural networks. In *International Conference on Machine Learning*, pages 3744–3753. PMLR, 2019. 5
- Bo Li. 3d fully convolutional network for vehicle detection in point cloud. In *2017 IEEE/RSJ International Conference on Intelligent Robots and Systems*, pages 1513–1518. IEEE, 2017. 4
- Yinhao Li, Zheng Ge, Guanyi Yu, Jinrong Yang, Zengran Wang, Yukang Shi, Jianjian Sun, and Zeming Li. Bevdepth: Acquisition of reliable depth for multi-view 3d object detection. *Proceedings of the AAAI Conference on Artificial Intelligence*, 37(2):1477–1485, 2023. 3
- Zhichao Li, Feng Wang, and Naiyan Wang. Lidar r-cnn: An efficient and universal 3d object detector. In *Proceedings of the IEEE/CVF Conference on Computer Vision and Pattern Recognition*, pages 7546–7555, 2021. 1, 2, 4, 12
- Zhiqi Li, Wenhui Wang, Hongyang Li, Enze Xie, Chonghao Sima, Tong Lu, Yu Qiao, and Jifeng Dai. Bevformer: Learning bird’s-eye-view representation from multi-camera images via spatiotemporal transformers. In *European conference on computer vision*, pages 1–18. Springer, 2022. 3
- Zhidong Liang, Zehan Zhang, Ming Zhang, Xian Zhao, and Shiliang Pu. RangeiouDET: Range image based real-time 3d object detector optimized by intersection over union. In *Proceedings of the IEEE/CVF Conference on Computer Vision and Pattern Recognition*, pages 7140–7149, 2021. 4
- Haisong Liu, Yao Teng, Tao Lu, Haiguang Wang, and Limin Wang. Sparsebev: High-performance sparse 3d object detection from multi-camera videos. In *Proceedings of the IEEE/CVF International Conference on Computer Vision*, pages 18580–18590, 2023a. 4
- Xianpeng Liu, Nan Xue, and Tianfu Wu. Learning auxiliary monocular contexts helps monocular 3d object detection. *arXiv preprint arXiv:2112.04628*, 2021a. 3
- Yingfei Liu, Tiancai Wang, Xiangyu Zhang, and Jian Sun. Petr: Position embedding transformation for multi-view 3d object detection. In *European Conference on Computer Vision*, pages 531–548. Springer, 2022. 4
- Yingfei Liu, Junjie Yan, Fan Jia, Shuailin Li, Aqi Gao, Tiancai Wang, and Xiangyu Zhang. PetrV2: A unified framework for 3d perception from multi-camera images. In *Proceedings of the IEEE/CVF International Conference on Computer Vision*, pages 3262–3272, 2023b. 4
- Yuxuan Liu, Yuan Yixuan, and Ming Liu. Ground-aware monocular 3d object detection for autonomous driving. *IEEE Robotics and Automation Letters*, 6(2):919–926, 2021b. 3
- Ze Liu, Yutong Lin, Yue Cao, Han Hu, Yixuan Wei, Zheng Zhang, Stephen Lin, and Baining Guo. Swin transformer: Hierarchical vision transformer using shifted windows. In *Proceedings of the IEEE/CVF International Conference on Computer Vision*, pages 10012–10022, 2021c. 4, 11
- Ze Liu, Zheng Zhang, Yue Cao, Han Hu, and Xin Tong. Group-free 3d object detection via transformers. In *Proceedings of the IEEE/CVF International Conference on Computer Vision*, pages 2949–2958, 2021d. 4
- Zechen Liu, Zizhang Wu, and Roland Tóth. Smoke: Single-stage monocular 3d object detection via keypoint estimation. In *Proceedings of the IEEE/CVF Conference on Computer Vision and Pattern Recognition Workshops*, pages 996–997, 2020. 3
- Yan Lu, Xinzhu Ma, Lei Yang, Tianzhu Zhang, Yating Liu, Qi Chu, Junjie Yan, and Wanli Ouyang. Geometry uncertainty projection network for monocular 3d object detection. In *Proceedings of the IEEE/CVF International Conference on Computer Vision (ICCV)*, pages 3111–3121, 2021. 3
- Xinzhu Ma, Zhihui Wang, Haojie Li, Pengbo Zhang, Wanli Ouyang, and Xin Fan. Accurate monocular 3d object detection via color-embedded 3d reconstruction for autonomous driving. In *Proceedings of the IEEE/CVF International Conference on Computer Vision (ICCV)*, pages 6851–6860, 2019. 3
- Xinzhu Ma, Shinan Liu, Zhiyi Xia, Hongwen Zhang, Xingyu Zeng, and Wanli Ouyang. Rethinking pseudo-lidar representation. In *European Conference on Computer Vision (ECCV)*, pages 311–327, 2020. 3
- Jiageng Mao, Yujing Xue, Minzhe Niu, Haoyue Bai, Jiashi Feng, Xiaodan Liang, Hang Xu, and Chunjing Xu. Voxel transformer for 3d object detection. In *Proceedings of the IEEE/CVF International Conference on Computer Vision*, pages 3164–3173, 2021. 4, 5, 12, 13
- Ishan Misra, Rohit Girdhar, and Armand Joulin. An end-to-end transformer model for 3d object detection. In *Proceedings of the IEEE/CVF International Conference on Computer Vision*, pages 2906–2917, 2021. 4

- Xuran Pan, Zhuofan Xia, Shiji Song, Li Erran Li, and Gao Huang. 3d object detection with pointformer. *arXiv preprint arXiv:2012.11409*, 2020. **5**
- Jonah Philion and Sanja Fidler. Lift, splat, shoot: Encoding images from arbitrary camera rigs by implicitly unprojecting to 3d. In *Computer Vision—ECCV 2020: 16th European Conference, Glasgow, UK, August 23–28, 2020, Proceedings, Part XIV 16*, pages 194–210. Springer, 2020. **3**
- Charles R Qi, Hao Su, Kaichun Mo, and Leonidas J Guibas. Pointnet: Deep learning on point sets for 3d classification and segmentation. In *Proceedings of the IEEE conference on computer vision and pattern recognition (CVPR)*, pages 652–660, 2017a. **1, 2, 4, 5**
- Charles Ruizhongtai Qi, Li Yi, Hao Su, and Leonidas J Guibas. Pointnet++: Deep hierarchical feature learning on point sets in a metric space. *Advances in Neural Information Processing Systems (NIPS)*, 30:5099–5108, 2017b. **5**
- Cody Reading, Ali Harakeh, Julia Chae, and Steven L Waslander. Categorical depth distribution network for monocular 3d object detection. In *Proceedings of the IEEE/CVF Conference on Computer Vision and Pattern Recognition (CVPR)*, pages 8555–8564, 2021. **3**
- Hualian Sheng, Sijia Cai, Yuan Liu, Bing Deng, Jianqiang Huang, Xian-Sheng Hua, and Min-Jian Zhao. Improving 3d object detection with channel-wise transformer. In *Proceedings of the IEEE/CVF International Conference on Computer Vision (ICCV)*, pages 2743–2752, 2021. **1, 2, 4, 5, 8, 9, 11, 13, 14**
- Hualian Sheng, Sijia Cai, Na Zhao, Bing Deng, Jianqiang Huang, Xian-Sheng Hua, Min-Jian Zhao, and Gim Hee Lee. Rethinking iou-based optimization for single-stage 3d object detection. In *Proceedings of the European Conference on Computer Vision*, pages 544–561. Springer, 2022. **1, 4, 8, 11, 12, 13, 14**
- Hualian Sheng, Sijia Cai, Na Zhao, Bing Deng, Min-Jian Zhao, and Gim Hee Lee. Pdr: Progressive depth regularization for monocular 3d object detection. *IEEE Transactions on Circuits and Systems for Video Technology*, 2023. **3**
- Shaoshuai Shi, Xiaogang Wang, and Hongsheng Li. Pointcnn: 3d object proposal generation and detection from point cloud. In *Proceedings of the IEEE Conference on Computer Vision and Pattern Recognition (CVPR)*, pages 770–779, 2019. **4, 5, 8**
- Shaoshuai Shi, Chaoxu Guo, Li Jiang, Zhe Wang, Jianping Shi, Xiaogang Wang, and Hongsheng Li. Pv-rcnn: Point-voxel feature set abstraction for 3d object detection. In *Proceedings of the IEEE/CVF Conference on Computer Vision and Pattern Recognition*, pages 10529–10538, 2020a. **1, 2, 4, 5, 8, 11, 12, 13, 14**
- Shaoshuai Shi, Zhe Wang, Jianping Shi, Xiaogang Wang, and Hongsheng Li. From points to parts: 3d object detection from point cloud with part-aware and part-aggregation network. *IEEE Transactions on Pattern Analysis and Machine Intelligence*, 43(8):2647–2664, 2020b. **13**
- Shaoshuai Shi, Li Jiang, Jiajun Deng, Zhe Wang, Chaoxu Guo, Jianping Shi, Xiaogang Wang, and Hongsheng Li. Pv-rcnn++: Point-voxel feature set abstraction with local vector representation for 3d object detection. *International Journal of Computer Vision*, 131(2):531–551, 2023. **1, 2, 4, 8, 11, 12, 13, 14**
- Xuepeng Shi, Qi Ye, Xiaozhi Chen, Chuangrong Chen, Zhixiang Chen, and Tae-Kyun Kim. Geometry-based distance decomposition for monocular 3d object detection. In *Proceedings of the IEEE/CVF International Conference on Computer Vision (ICCV)*, pages 15172–15181, 2021. **3**
- Minsoo Song, Seokjae Lim, and Wonjun Kim. Monocular depth estimation using laplacian pyramid-based depth residuals. *IEEE Transactions on Circuits and Systems for Video Technology (TCSVT)*, 31(11):4381–4393, 2021. **3**
- Shuran Song and Jianxiong Xiao. Deep sliding shapes for amodal 3d object detection in rgb-d images. In *Proceedings of the IEEE Conference on Computer Vision and Pattern Recognition (CVPR)*, pages 808–816, 2016. **5**
- OpenPCDet Development Team. Openpcdet: An open-source toolbox for 3d object detection from point clouds. <https://github.com/open-mmlab/OpenPCDet>, 2020. **11**
- Hugo Touvron, Matthieu Cord, Matthijs Douze, Francisco Massa, Alexandre Sablayrolles, and Hervé Jégou. Training data-efficient image transformers & distillation through attention. In *International Conference on Machine Learning*, pages 10347–10357. PMLR, 2021. **4**
- Ashish Vaswani, Noam Shazeer, Niki Parmar, Jakob Uszkoreit, Llion Jones, Aidan N Gomez, Lukasz Kaiser, and Illia Polosukhin. Attention is all you need. In *Advances in Neural Information Processing Systems (NIPS)*, pages 5998–6008, 2017. **2, 3, 4, 9, 15**
- Apoorv Vyas, Angelos Katharopoulos, and François Fleuret. Fast transformers with clustered attention. *Advances in Neural Information Processing Systems*, 33:21665–21674, 2020. **10**
- Li Wang, Li Zhang, Yi Zhu, Zhi Zhang, Tong He, Mu Li, and Xiangyang Xue. Progressive coordinate transforms for monocular 3d object detection. *Advances in Neural Information Processing Systems (NeurIPS)*, 34, 2021a. **3**
- Sinong Wang, Belinda Z Li, Madian Khabsa, Han Fang, and Hao Ma. Linformer: Self-attention with linear complexity. *arXiv preprint arXiv:2006.04768*, 2020. **2, 10**
- Tai Wang, Xinge Zhu, Jiangmiao Pang, and Dahua Lin. Fcos3d: Fully convolutional one-stage monocular 3d object detection. In *Proceedings of the IEEE/CVF International Conference on Computer Vision (ICCV)*, pages 913–922, 2021b. **3**
- Yan Wang, Wei-Lun Chao, Divyansh Garg, Bharath Hariharan, Mark Campbell, and Kilian Q Weinberger. Pseudolidar from visual depth estimation: Bridging the gap in 3d object detection for autonomous driving. In *Proceedings of the IEEE/CVF Conference on Computer Vision and Pattern Recognition (CVPR)*, pages 8445–8453, 2019. **3**
- Yue Wang, Vitor Campagnolo Guizilini, Tianyuan Zhang, Yilun Wang, Hang Zhao, and Justin Solomon. Detr3d: 3d object detection from multi-view images via 3d-to-2d queries. In *Conference on Robot Learning*, pages 180–191. PMLR, 2022. **4**
- Qiangeng Xu, Yiqi Zhong, and Ulrich Neumann. Behind the curtain: Learning occluded shapes for 3d object detection. *Proceedings of the AAAI Conference on Artificial Intelligence*, 36(3):2893–2901, 2022. **1, 4, 11, 12, 13**
- Yan Yan, Yuxing Mao, and Bo Li. Second: Sparsely embedded convolutional detection. *Sensors*, 18(10):3337, 2018. **1, 2, 4, 5, 8, 11, 13**
- Bin Yang, Wenjie Luo, and Raquel Urtasun. Pixor: Real-time 3d object detection from point clouds. In *Proceedings of the IEEE conference on Computer Vision and Pattern Recognition (CVPR)*, pages 7652–7660, 2018. **4**
- Chenyu Yang, Yuntao Chen, Hao Tian, Chenxin Tao, Xizhou Zhu, Zhaoxiang Zhang, Gao Huang, Hongyang Li, Yu Qiao, Lewei Lu, et al. Bevformer v2: Adapting modern image backbones to bird’s-eye-view recognition via perspective supervision. In *Proceedings of the IEEE/CVF Conference on Computer Vision and Pattern Recognition*, pages 17830–

- 17839, 2023. 3
- Zetong Yang, Yanan Sun, Shu Liu, and Jiaya Jia. 3dssd: Point-based 3d single stage object detector. In *Proceedings of the IEEE/CVF Conference on Computer Vision and Pattern Recognition*, pages 11040–11048, 2020. 4, 13
- Tianwei Yin, Xingyi Zhou, and Philipp Krahenbuhl. Center-based 3d object detection and tracking. In *Proceedings of the IEEE/CVF Conference on Computer Vision and Pattern Recognition (CVPR)*, pages 11784–11793, 2021. 1, 2, 4, 12
- Renrui Zhang, Han Qiu, Tai Wang, Ziyu Guo, Ziteng Cui, Yu Qiao, Hongsheng Li, and Peng Gao. Monodetr: Depth-guided transformer for monocular 3d object detection. In *Proceedings of the IEEE/CVF International Conference on Computer Vision*, pages 9155–9166, 2023. 3
- Yifan Zhang, Qingyong Hu, Guoquan Xu, Yanxin Ma, Jianwei Wan, and Yulan Guo. Not all points are equal: Learning highly efficient point-based detectors for 3d lidar point clouds. In *Proceedings of the IEEE/CVF Conference on Computer Vision and Pattern Recognition*, pages 18953–18962, 2022. 12
- Yunpeng Zhang, Jiwen Lu, and Jie Zhou. Objects are different: Flexible monocular 3d object detection. In *Proceedings of the IEEE/CVF Conference on Computer Vision and Pattern Recognition (CVPR)*, pages 3289–3298, 2021. 3
- Hengshuang Zhao, Li Jiang, Jiaya Jia, Philip HS Torr, and Vladlen Koltun. Point transformer. In *Proceedings of the IEEE/CVF International Conference on Computer Vision*, pages 16259–16268, 2021. 4
- Wu Zheng, Weiliang Tang, Sijin Chen, Li Jiang, and Chi-Wing Fu. Cia-ssd: Confident iou-aware single-stage object detector from point cloud. *Proceedings of the AAAI Conference on Artificial Intelligence*, 35(4):3555–3562, 2021. 1, 4, 5, 8
- Xingyi Zhou, Jiacheng Zhuo, and Philipp Krahenbuhl. Bottom-up object detection by grouping extreme and center points. In *Proceedings of the IEEE Conference on Computer Vision and Pattern Recognition (CVPR)*, pages 850–859, 2019. 5
- Yin Zhou and Oncel Tuzel. Voxelnet: End-to-end learning for point cloud based 3d object detection. In *Proceedings of the IEEE/CVF Conference on Computer Vision and Pattern Recognition*, pages 4490–4499, 2018. 4, 5, 13